https://doi.org/10.5194/egusphere-2024-2155
Preprint. Discussion started: 19 August 2024

Variations in the microstructure of saline ice during its growth and decay: Evidences from an experimental study

Miao Yu[1,2], Peng Lu[1*], Hang Zhang[1], Fei Xie[1], Lei Wang[3], Qingkai Wang[1], Zhijun Li[1]

[1] State Key Laboratory of Coastal and Offshore Engineering, Dalian University of Technology, Dalian 116024, China
[2] School of Naval Architecture Engineering, Dalian University of Technology, Dalian, China
[3] School of Mathematical Sciences, Dalian University of Technology, Dalian, China

Correspondence to: Peng Lu (lupeng@dlut.edu.cn)

Abstract. Ice physics are highly sensitive to the ice temperature and are primarily determined by the distribution of inclusions such as gas bubbles and brine pockets within ice. However, a detailed understanding of their distributions and evolution patterns during ice freezing and melting is lacking. To address this issue, in situ experiments were conducted to collect detailed information on the variations in the microstructure of ice using continuous sampling and a high-resolution imaging system. The results revealed a 5- to 10-fold increase in the volume fraction and a 2-fold increase in the size of gas bubbles during the melting phase of ice. Moreover, the size of brine pockets in the ice surface, middle, and bottom layers clearly increased for different reasons. The nearly 30% increase in gas bubbles observed in the middle layer was thermally driven, while the increase in the surface layer was influenced by the net shortwave radiation. Additionally, the variation in the inclusion size distribution was attributed to the merging process, most of which occurred among smaller inclusions rather than among larger inclusions. The changing ice temperature is a significant factor in the merging process of the middle layer but not for the surface or bottom layers. This study could enhance the understanding of the effect of the transfer of energy between the atmosphere and water beneath ice on the ice microstructure.

1 Introduction

Ice is a multiphase material comprising ice crystals, gas bubbles, and impurities (Hruba and Kletetschka, 2018; Hunke et al., 2011; Petrich and Eicken, 2017). Saline ice also contains brine pockets or salt precipitates (Light et al., 2003; Notz and Worster, 2008). The proportions of these components vary with the ice formation, freezing, and melting phases (Eicken, 2003; Frantz et al., 2019; Light et al., 2003; Perovich and Gow, 1996). Therefore, the properties of bulk ice, including thermal, optical, electromagnetic, and mechanical properties, exhibit significant variability in both time and space (Light et al., 2008; Pringle et al., 2009; Wang et al., 2020). As a result, ice plays a crucial role in the transfer of heat, salt, gases, and radiation between subglacial water and the atmosphere (Corkill et al., 2023; Crabeck et al., 2014; Light et al., 2004; Trodahl et al., 2001; Vancoppenolle et al., 2010), rendering it a key element of the Earth's climate system.

Variations in the inclusions within natural ice depend on two main factors: the meteorological environment and the hydrographic boundary conditions (Eicken, 2003). The content of newly formed brine pockets in ice can be quantified by an

https://doi.org/10.5194/egusphere-2024-2155
Preprint. Discussion started: 19 August 2024

effective segregation coefficient and the salinity of the underlying water (Cox and Weeks, 1988). Moreover, the formation of gas bubbles in ice is related to many factors (Tsurikov, 1979). During the initial freezing phase, gases are released from the solution and trapped in the initial ice cover, referred to as inactive bubbles by Light et al. (2004). Additionally, as the ice temperature changes, the volume of brine pockets and gas bubbles changes as a result of phase variations to maintain gas–brine equilibrium (Crabeck et al., 2019). For example, voids form due to the partial evaporation of ice or brine during internal melting. Notably, Light et al. (2004) defined these bubbles affected by the melting process as active bubbles.

A statistical description of how the volume of inclusions changes is needed to better understand how the physical properties of ice change. Based on ice phase diagrams (Cox and Weeks, 1983; Leppäranta and Manninen, 1988), the seasonal and annual variations in bubbles and brine volumes in ice can be obtained. The results indicate a significant increase in ice porosity during the melting season (Salganik et al., 2023; Wang et al., 2020). The latest mushy layer theory was employed as the physical basis for brine exchange processes in ice and could be used to simulate the changing V_b value of ice (Bailey et al., 2020; Hunke et al., 2011; Turner and Hunke, 2015). The variations in the V_b profile were clearly impacted by ice surface radiation (Vancoppenolle et al., 2007). During the Multidisciplinary drifting Observatory for the Study of the Arctic Climate expedition (MOSAiC), Macfarlane et al. (2023) reported the seasonal variation in the specific surface area of the ice surface scattering layer.

The morphology of ice inclusions is another significant property that should be observed. Grenfell (1983) and Perovich and Gow (1996) reported the size and distribution of gas bubbles in sea ice. Cole and Shapiro (1998) recorded detailed information on the size and shape of brine inclusions. Recent studies on the inclusion morphology have largely focused on their connection with ice physical changes, providing useful information. For example, studies have shown that the size of inclusions increases in the melting process due to the aqueous–gaseous equilibrium (Frantz et al., 2019; Light et al., 2003), while the number of inclusions decreases (Salomon et al., 2022). Additionally, the ice texture (granular or columnar) is an important factor controlling the gas size distribution (Crabeck et al., 2016; Oggier and Eicken, 2022).

Although previous observations have provided a general understanding of the ice microstructure, there is limited available information on the exact seasonal variation in inclusions. Some studies on changes in the inclusion size distribution mainly rely on laboratory cooling or heating processes (Crabeck et al., 2019; Light et al., 2003), which may not accurately represent the physics of natural ice changes with radiation and other meteorological factors. Due to the lack of seasonal variations in ice inclusions, it remains challenging to precisely obtain variations in ice physical properties. This inevitability introduces inaccuracies into ice models in response to varying circumstances. In this study, for the first time, high-resolution imagery was used to observe the microstructure of natural saline ice throughout the winter season together with its physical properties. The temporal variations and vertical distributions of the size and volume fractions of inclusions were investigated, while the factors driving these variations were also explored.

https://doi.org/10.5194/egusphere-2024-2155
Preprint. Discussion started: 19 August 2024

2 Fieldwork and methods

Field observations were conducted in Lake Hanzhang, which is a brackish water body that originates from the Bohai Sea (Figure 1a, b), from December 1, 2022, to February 23, 2023. The lake water salinity ranged from approximately 5–7‰. The freezing period typically lasts for 3-4 months, from early December to mid-March. A floating remote observation system (Figure 1c) was deployed prior to ice formation and recovered after complete ice melting at the site (Xie et al., 2022). Then, the ice properties, meteorological data, and water properties under the overall seasonal variations in ice could be measured. Ice cores were obtained near the floating platform approximately once a week to analyse the ice density, salinity, and microstructure when the ice thickness was large enough. A total of 7 samples were collected during the observation, and the distance between the sampling sites was no more than 20 cm to avoid the effects of spatial differences.

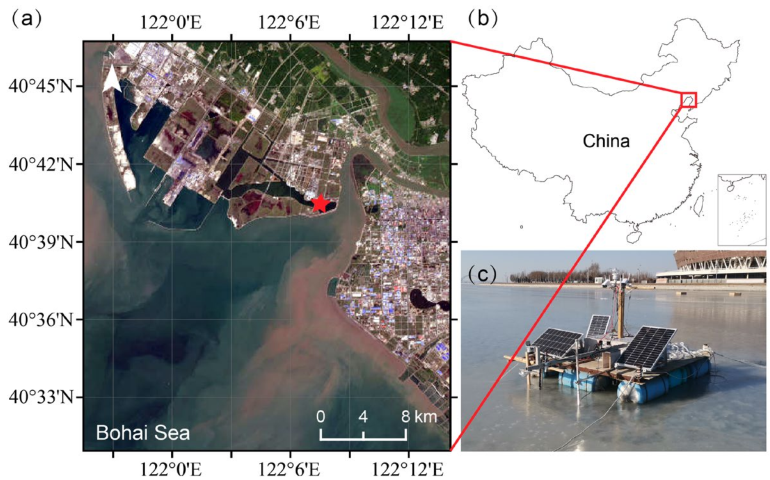

Figure 1: (a, b) Fieldwork site (shown as a red star) and (c) the floating remote observation system. The base map in (a) is imagery satellite from TerraColor NextGen obtained on January 11, 2023.

2.1 Ice physics

The ice thickness was measured using an ultrasonic sensor (PA500, Tritech, Westhill, UK), with a measuring range of 0.1 to 10 m, a 1-mm resolution, and a 2.5-mm accuracy. The ultrasound sensor was affixed onto the floating platform and maintained upright in water. The ice thickness was then calculated by subtracting the distance between the ice bottom and the sensor from the known distance between the ice surface and the sensor. The ice surface height was monitored using a downward ultrasonic sensor (SR50A, Campbell Scientific, Logan, UT, USA), with a measuring range of 0.5–10 m and an accuracy of 1 cm.

Platinum resistance sensors (PTWD, Sunshine Meteorological Technology (Jinzhou) Ltd., Jinzhou, China) were employed to measure the vertical temperature profiles of ice and water. The available temperature measurement range is from −40°C to

https://doi.org/10.5194/egusphere-2024-2155
Preprint. Discussion started: 19 August 2024

+150°C, with a precision of 0.04°C. The sensors were calibrated using an ice/distilled water mixture at 0°C prior to the experiment. A wooden frame was used to fix the probes at 3-cm intervals on ice. As wood exhibits a lower thermal conductivity than ice (Hruba and Kletetschka, 2018), the impact of the frame on our observations was neglected. The temperature of the ice surface was measured using an infrared temperature sensor (SI-411, Apogee Instruments, Logan, UT, USA), with an accuracy of 0.2°C.

After extracting ice samples at each sampling site, a portion of each sample was immediately cut into 5-cm sections and stored in sealed plastic containers to thaw. The bulk salinity of the meltwater was obtained using a salinometer, with an accuracy of 0.1‰. The other sample portion was used to measure the ice density according to Archimedes' law, which exhibits a lower measurement uncertainty than the most common mass/volume method (Pustogvar and Kulyakhtin, 2016). The sample mass was measured both while floating on and while submerged in cold antifreeze liquid to prevent the ice from melting during the measurement. Then, the ice density (ρ_{ice}) can be derived as follows:

$$\rho_{\text{ice}} = \frac{M_2 - M_1}{M_3 - M_1} \rho_{\text{l}} \tag{1}$$

where M_1 is the total mass of the container and the contained liquid, M_2 is the total mass of the container when the ice sample floats on the liquid, M_3 is the total mass of the container when the ice sample is immersed in the liquid, and ρ_{l} is the known density of the antifreeze liquid. In the following analysis, the first 5-cm layer of ice was defined as the surface layer, and the last 5-cm layer was defined as the bottom layer. The remaining section was defined as the middle layer.

2.2 Meteorological conditions

The meteorological conditions were monitored on an hourly basis using a compact weather station (MaxiMet GMX 501, Gill Instruments Ltd., Lymington, UK). The available parameters included the shortwave solar radiation, air temperature, relative humidity, wind speed and direction, with corresponding accuracies of 1 W m^{-2}, 0.3°C, 2%, 3%, and 3°, respectively.

The incident shortwave radiation can be obtained from weather stations. Another global radiometer (TBQ-2, Sunshine Meteorological Technology (Jinzhou) Ltd., Jinzhou, China) was arranged above the ice surface to monitor the total reflected shortwave radiation. The radiometer was placed on an extension rod away from the floating platform to prevent any possible influence of platform shadows.

The net longwave radiation (Q_{ln}) is the difference between the downwelling longwave radiation (Q_{ld}) and upwelling longwave radiation (Q_{lu}), which can be obtained as follows:

$$Q_{ln} = Q_{ld} - Q_{lu} = \varepsilon_a \sigma T_a^4 - \varepsilon \sigma T_0^4 \tag{2}$$

where σ is the Stefan–Boltzmann constant (5.67×10^{-8} W m^{-2} K^{-1}), T_{a} and T_0 are the air temperature and ice surface temperature, respectively, ε is the ice surface emissivity (0.98), and ε_{a} is the effective atmospheric emissivity, which depends on the humidity and cloudiness (Efimova, 1961):

$$\varepsilon_a = (A + B \cdot e)(1 + C \cdot N^2) \tag{3}$$

https://doi.org/10.5194/egusphere-2024-2155
Preprint. Discussion started: 19 August 2024

where A and B are clear sky parameters (A = 0.746 and B = 0.0066), e is the water vapor pressure, which is a function of the temperature, C is the cloudiness coefficient (0.26), and N is the cloudiness, which can be estimated by the difference between the theoretical clear sky irradiance (Meyers and Dale, 1983) and the measured irradiance (Crawford and Duchon, 1999). This parameterization agrees well with the observed results (Duarte et al., 2006).

2.3 Ice microstructure

2.3.1 Volume fraction of inclusions

In this study, V_a and V_b of ice were calculated according to phase diagrams (Cox and Weeks, 1983; Leppäranta and Manninen, 1988) using in situ ice temperature (T), bulk ice salinity (S), and bulk ice density (ρ_{ice}) measurements of the ice samples:

$$V_a = 1 - \frac{\rho_{ice}}{\rho_i} + \rho S \frac{F_2}{F_1} \tag{4}$$

$$V_b = \frac{\rho_{ice} S}{F_1} \tag{5}$$

where ρ_i is the density of pure ice (Cox and Weeks, 1983):

$$\rho_i = 0.917 - 1.403 \times 10^{-4} \times T \tag{6}$$

F_1 and F_2 are also functions of the ice temperature. Here, T was obtained from the vertical temperature profile (Section 2.1). The temperature profile of the original ice was interpolated from 3- to 1-cm intervals. This allowed for calculating the mean ice temperature for each 5-cm layer.

2.3.2 Size of inclusions

The ice samples were processed into vertical thin sections with a thickness of ~5 mm to observe their microstructure. This thickness was chosen to ensure that the individual inclusions were entirely visible and not obscured by others. Subsequently, the thin ice sections were imaged in a cold laboratory (-10°C) for inclusion observation. To enhance the visibility of gas bubbles and brine pockets and to facilitate image processing, the thin sections were imaged under diffuse light. Each typical image covers an area of approximately 2 × 3 mm. Notably, the true length of a pixel is approximately 0.002 mm, while higher-resolution images were obtained at a resolution of 0.001 mm per pixel. Approximately 30–70 images were recorded for each thin section within ~5 min. In total, more than 1800 images were recorded covering all ice samples. The potential effect of the low temperature in the cold laboratory on the ice microstructure during imaging is described in Section 4.1.

After obtaining thin section photographs, they were analyzed using ImageJ software (rsb.info.nih.gov/ij/). The first step involved image filtering by applying a Gaussian blur filter (standard deviation 100) to obtain a background image. The background image was then subtracted from the original image to eliminate the effect of unfocused inclusions. Next, image segmentation was performed by exploiting the grey level differences between ice and inclusions. Many automated

https://doi.org/10.5194/egusphere-2024-2155
Preprint. Discussion started: 19 August 2024

segmentation algorithms have been adopted in related studies. The Ostu algorithm (Otsu, 1979) was used by Maus et al. (2021). Crabeck et al. (2021) employed the Ridler method (Ridler and Calvard, 1978) to separate background and inclusion pixels. Several segmentation methods were assessed on our ice image sets to ensure a stable algorithm response. Then, the results of each segmentation method were visually evaluated by comparing the raw and segmented images. The segmentation threshold produced by the Ridler method facilitated the accurate identification of inclusions in all images while introducing minimal noise in the segmented image. Moreover, the batch-segmented images were manually verified. Several images were randomly selected, and the background and inclusions were manually separated. The obtained batch-segmented inclusions were slightly larger than the manually segmented inclusions, with a mean difference of 5 pixels, equivalent to approximately 0.008 mm.

Following image partitioning, the inclusions were categorized as either gas bubbles or brine pockets. The observation of Perovich and Gow (1996) regard all inclusions in first-year ice are brine pockets, whereas all inclusions in multiyear ice are gas bubbles. Light et al. (2003) empirically classified inclusions based on their shape. Notably, brine pockets are trapped between ice platelets, and they move and become elongated as ice grows and melts (Petrich and Eicken, 2017). The shape of most brine pockets is heterogeneous, but most gas bubbles are nearly spherical (Crabeck et al., 2019; Light et al., 2003). Therefore, gas bubbles and brine pockets were classified based on the circularity ($4\pi \times \frac{area}{\text{perimeter}^2}$) of the inclusions (Figure 2). Several circularity thresholds were tested for our ice image sets, and inclusions with a circularity greater than 0.75 were regarded as gas bubbles. The Spearman correlation coefficient between V_a derived from the images and that calculated from the phase diagrams was 0.78 ($p < 0.001$), which indicates that the tendencies of V_a obtained from the two methods were significantly related. Note that the transparent portions of thin sections devoid of inclusions were discarded during imaging. Therefore, the V_a values derived from the images were greater than the real values. Therefore, V_a calculated from the images was not employed in this study.

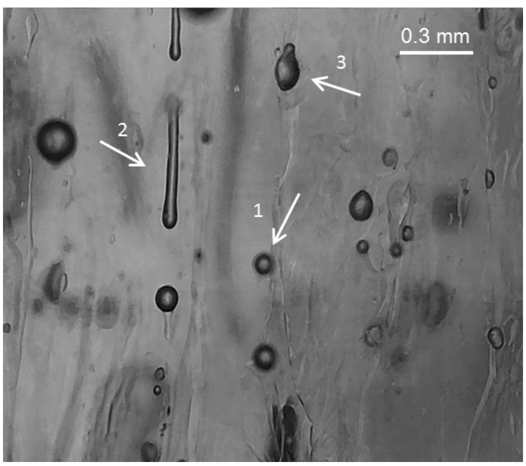

Figure 2: Image of a vertical thin section of ice. The arrows indicate examples of (1) gas bubbles and (2, 3) brine pockets.

https://doi.org/10.5194/egusphere-2024-2155
Preprint. Discussion started: 19 August 2024

Following Grenfell (1983) and Light et al. (2003), the size distribution function of the inclusions was defined as the number of inclusions per mm^3 per unit length. Unless otherwise specified, the bubble size in this study refers to the diameter, while the brine pocket size refers to the length, i.e., the maximum caliper length. The raw inclusion size data were binned by size, with bin widths of 0.01 mm for gas bubbles and 0.05 mm for brine pockets. The mean number of gas bubble bins was 70, while the mean value of brine pocket bins was 50. These data were sufficient for analysing the inclusion size distribution, and outliers could be avoided.

3 Results

3.1 General conditions during the ice season

3.1.1 Weather conditions

Figure 3 shows the weather conditions during the observation period, with the grey columns indicating the sampling dates. Here, the period from January 1 to February 23 was emphasized because the unshown and sampling dates greatly differed. The weather conditions throughout the whole ice season are shown in Figure S1. Throughout the observation period, there were no snowfall or rainfall events. Additionally, there was an increasing trend in the incident shortwave irradiance (Pearson correlation coefficient r = 0.65, p < 0.001). During the later phase of the observation period, the downwelling shortwave irradiance reached 180 W m^{-2}. The ambient air temperature varied between 0 and -16°C, with an average temperature of -3.7°C. Figure 3b shows the minimum air temperature on January 23. Subsequently, the air temperature gradually increased until the end of the observation period (r = 0.53, p < 0.005). The humidity during the observed period was 65.3±14.8%, without a clear trend. Additionally, no clear wind speed or direction trends were observed. On most observation dates, the speed was lower than 3 m/s, and the corresponding wind direction remained relatively steady.

https://doi.org/10.5194/egusphere-2024-2155
Preprint. Discussion started: 19 August 2024

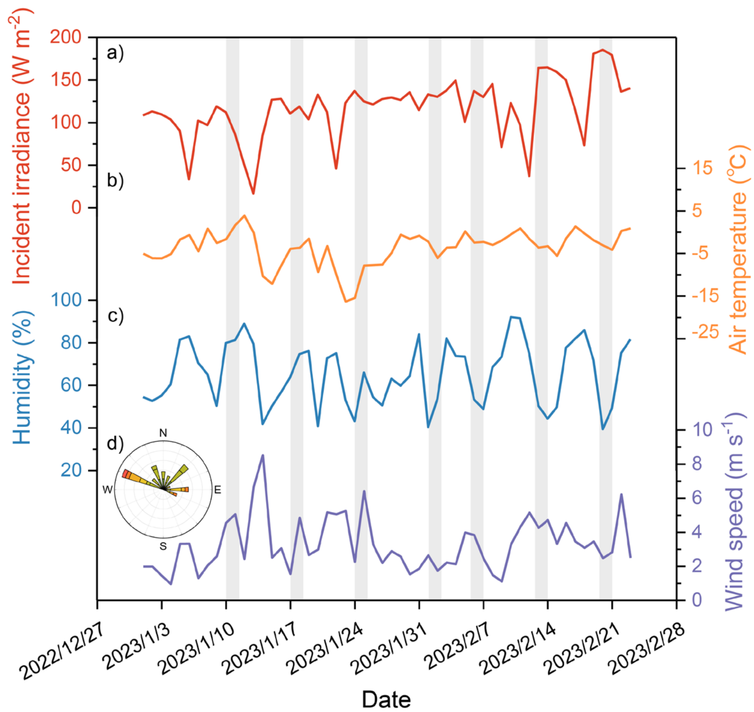

Figure 3: a) Incident irradiance, b) air temperature, c) humidity, d) wind speed and direction during the observation period from January 1 to February 23. The grey columns denote the ice sampling dates.

3.1.2 Ice thickness

The first time when the ultrasonic sensor detected ice formation was December 8, 2022 (Figure S1). Over the following 20 days, the ice thickness rapidly increased at a rate of 1.2 cm day^{-1} (r = 0.99, p < 0.001). By December 28, the ice thickness had reached 22.8 cm. Then, the growth rate decreased to 0.17 cm day^{-1} (r = 0.85, p < 0.001) from December 28, 2022, to January 31, 2023 (Figure 4). In February 2023, the ice thickness began to decrease. During the first two weeks, the melting rate reached 0.25 cm day^{-1} (r = -0.92, p < 0.001). Then, the rate increased to 3.3 cm day^{-1} (r = -0.94, p < 0.001) over the following days.

The variation in the ice surface elevation obtained from the downward ultrasonic sensor was not significant (-0.08 ± 0.5 cm, not shown in the figure), indicating that the ice surface did not move appreciably during the observation period. This could be attributed to the absence of snowfall or rainfall during the experiment, as well as unclear melting of the ice surface. As shown in Figure 4, the thickness of the ice samples agreed well with the ultrasonic sensor data (r = 0.96, p < 0.001). The mean difference was 1.1 cm, indicating that the ice surrounding the floating platform remained relatively level with no notable spatial variations. Therefore, the data obtained from the floating platform could be used in ice sample analysis.

https://doi.org/10.5194/egusphere-2024-2155
Preprint. Discussion started: 19 August 2024

3.1.3 Ice physics

The ice temperature of the ice samples varied between -7.5 and -0.06°C. The bulk temperature of the ice sampled on January 11 was -0.8°C, and it decreased to -3.8°C on January 25. The bulk temperature of the following three ice samples reached -1.4°C, with no clear changes. The ice sample collected on February 20 notably melted, with a bulk temperature of -0.8°C. All ice temperature profiles decreased from the surface to the bottom. The surface layer temperature showed similar temporal variations to those in the bulk temperature (r = 0.96, p < 0.001) and was significantly correlated with the air temperature (r = 0.95, p < 0.001). Moreover, the temperature of the bottom layer remained relatively stable (-0.4°C), except for the sample obtained on February 20 (-0.06°C). According to the variations in the ice temperature and thickness, the first three samples were considered to occur during the freezing phase, while the latter four samples were considered to occur during the melting phase (Figure 4).

The bulk salinity of the ice sample differed between the freezing and melting phases. The values were 0.61‰ and 0.37‰, respectively. All seven samples exhibited a nearly fresh surface layer. Most samples exhibited a maximum salinity in the middle layer, but the maximum salinity occurred in the bottom layer of the sample collected on February 20. Furthermore, the maximum salinity of each ice sample decreased (r = -0.89, p < 0.01). The bulk ice density ranged from 0.90 to 0.92 g cm^{-3}. The value remained nearly constant (0.91 g cm^{-3}) during the freezing phase and clearly decreased during the melting phase. On February 20, a significant melting event caused a high density (0.94 g cm^{-3}) in the bottom layer of ice, which was visibly saturated with water during sampling.

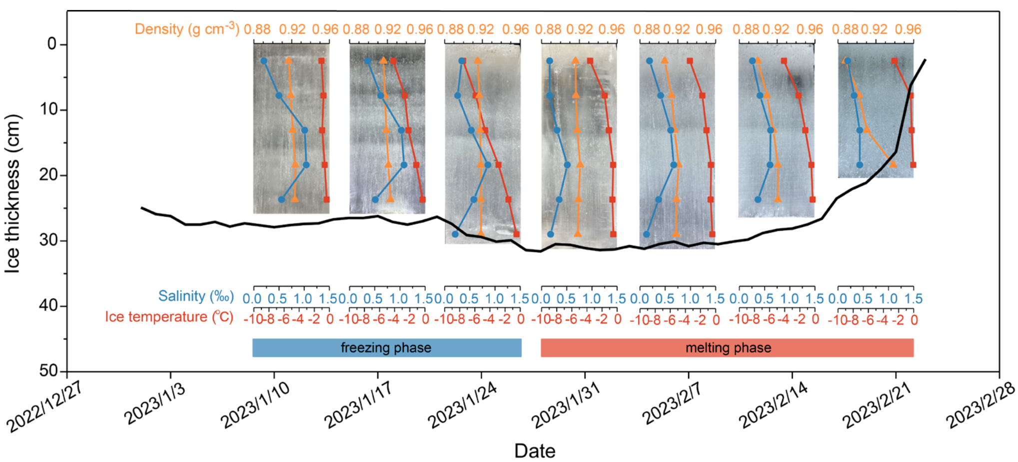

Figure 4: Observed variations in the ice thickness and sampled ice images overlain by the ice temperature, salinity, and density. Seven ice samples were sorted into the freezing and melting phases according to their temperature and thickness changes. The dates on the horizontal axis are formatted as year/month/day.

https://doi.org/10.5194/egusphere-2024-2155
Preprint. Discussion started: 19 August 2024

3.2 Ice microstructure

3.2.1 Variations in the volume fraction of inclusions

The volume fraction of gas bubbles (V_a) ranged from 0.1% to 3.3%. The brine pocket volume fraction (V_b) ranged from 0.3%–39.9%. Figure 5a shows that V_a during the freezing phase remained relatively stable. The mean V_a values for the surface, middle and bottom layers during the freezing phase were 0.3%, 0.1% and 0.05%, respectively. Subsequently, V_a clearly increased during the following melting phase. On February 20, there was a more than tenfold increase in V_a for the surface and middle layers compared to those of the ice sample collected on February 1. Additionally, the bottom layer experienced a fivefold increase.

In contrast, the observed V_b trends differed. Notably, V_b decreased in all three layers during the freezing phase and increased during the melting phase (Figure 5a). Among the three layers, the surface layer experienced the smallest decrease in V_b during the freezing phase. For the middle layer, the V_b value on January 25 was ~1/5 of that on January 11. A similar trend was also observed for the bottom layer. During the melting phase, the bottom layer showed the clearest increase in V_b, increasing from 1.8% on February 1 to 39.9% on February 20. The corresponding increase in the middle layer ranged from 2.3% to 5.9%. In summary, V_b of the middle and bottom layers was more sensitive to the freezing/melting phase than was that of the surface layer.

As ice melts, in a closed system, some of the pure ice surrounding each brine inclusion melts and becomes brine. Due to the greater density of brine than that of pure ice, gas bubbles expand to fill the volume difference. Therefore, changes in V_a are likely related to changes in V_b (Light et al., 2004). This relationship can be expressed as the melting equilibrium relationship (Cox and Weeks, 1983): $\Delta V_a = \Delta V_b (\rho_s / \rho_i - 1)$, where ρ_i is the density of pure ice (Equation 6), and ρ_s is the density of brine, which can be obtained according to the method of Maykut and Light (1995). According to the ice temperature during the observation period, the corresponding melting equilibrium is shown as a grey shaded area in Figure 5b.

The relationships between V_a and V_b for the different ice layers varied (Figure 5b). For the ice surface layer, V_a clearly increased with a low variation in V_b, resulting in a slope of the fitting line that was much lower than that of the melting equilibrium curve. This reveals that these newly formed gas bubbles did not result from the thermodynamic melting of pure ice. In contrast, for the bottom layer, there was high variation in V_b, but V_a remained relatively constant. The fitting line is distant from the melting equilibrium curve. From February 13 to 20, the increase in V_b was expected to result in a 3.1% increase in V_a. However, this phenomenon was not observed.

The general trend in V_b/V_a of the middle layer was more closely related to the melting equilibrium than that of the surface and bottom layers. During the melting phase of the middle layer (marked as ellipses in Figure 5b), the slope of V_b/V_a was 2.12 ($r = 0.93$, $p < 0.01$), which is lower than the thermodynamic equilibrium value. This indicates that ~30% of the increase in V_a could be explained by the change in V_b. The results for the middle layer during the freezing phase differed from those during the melting phase but were more similar to those for the bottom layer. The decrease in V_b from 5.5% on January 11 to 1.0% on January 25 did not result in clear V_a changes.

https://doi.org/10.5194/egusphere-2024-2155
Preprint. Discussion started: 19 August 2024

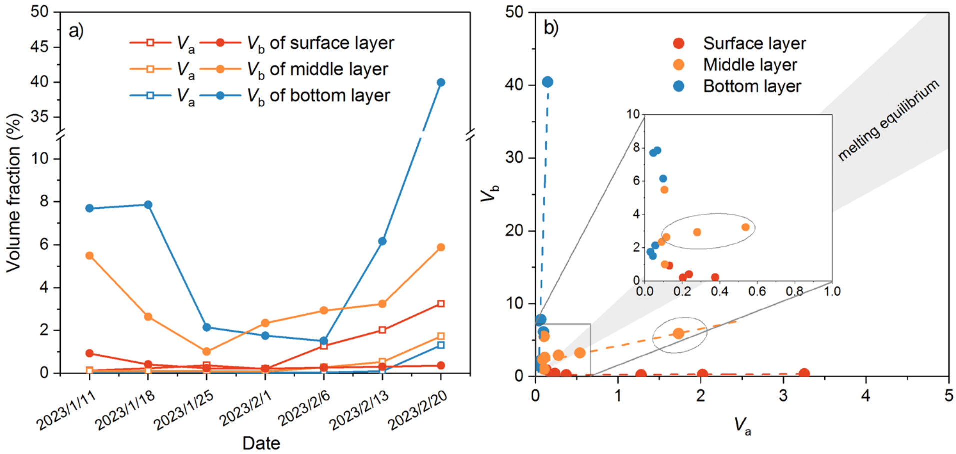

Figure 5: a) Temporal variations in the volume fractions of gas bubbles and brine pockets. b) Relationship between the brine and gas bubble volume fractions. The grey shaded area denotes the melting equilibrium relationships of Cox and Weeks (1983). The ellipses denote the results for the middle layer during the melting phase.

3.2.2 Variations in the size of inclusions

Figure 6a shows the interquartile range (IQR) box plot of the inclusion size for the different ice layers. The brine pockets were larger than the gas bubbles, while the brine pocket size range was also greater. The mean size of the gas bubbles in the surface layer was 0.07 mm, while in the middle and bottom layers, the corresponding values were 0.09 and 0.05 mm, respectively. Moreover, the mean sizes of the brine pockets in the surface, middle, and bottom layers were 0.33, 0.40, and 0.28 mm, respectively. The medians of the inclusion sizes were smaller than the corresponding means, except the brine pocket size in the bottom layer, where the median reached 0.5 times the mean. For the other layers, the median was ~0.6 times the corresponding mean. This indicates that most inclusion sizes were relatively small.

Figure 6b shows the cumulative number density of inclusions of different sizes in the different ice layers. The median sizes of the gas bubbles and brine pockets are shown as grey lines. Hereinafter, the inclusions with sizes smaller (larger) than their median were defined as small (large) inclusions. The size of the gas bubbles ranged from 0.002–3.17 mm, with half of the bubbles smaller than 0.05 mm. For the surface layer, 19% of the bubbles were larger than 0.1 mm. The corresponding proportions for the middle and bottom layers were 27% and 6%, respectively. This explains why the mean bubble size of the middle layer was larger than that of the surface and bottom layers (Figure 6a). A similar phenomenon was also observed for the brine pockets. The proportion of large brine pockets in the middle layer was greater than that in the surface and bottom layers.

https://doi.org/10.5194/egusphere-2024-2155
Preprint. Discussion started: 19 August 2024

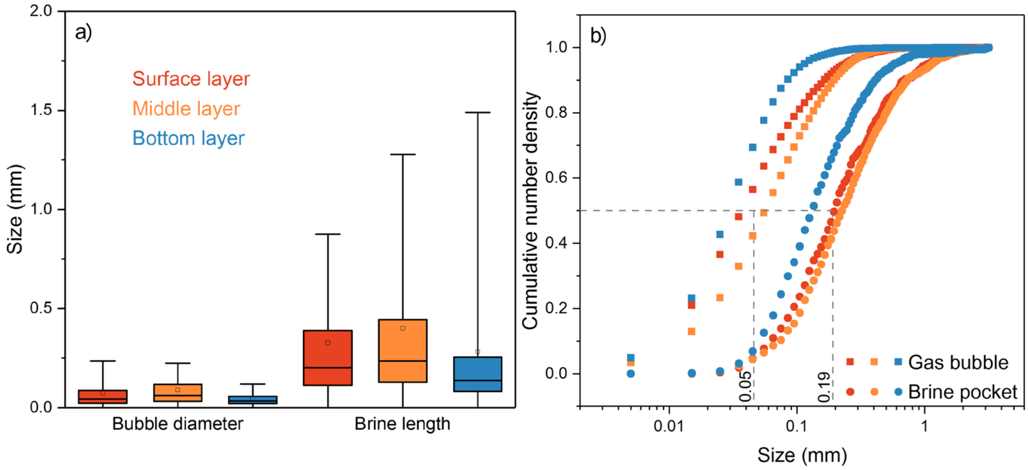

Figure 6: a) IQR box plot showing the distribution of the bubble diameter and brine pocket length. The box is defined by the first and third quartiles of the distribution. The line in the box is the median, and the square denotes the mean. b) Cumulative number density of the inclusions in the different ice layers. The grey lines denote the median of each inclusion size class.

Figure 7 shows the temporal variations in the inclusion sizes for the different ice layers and the proportion of large inclusions on each sampling date. There was a general increasing trend in the gas bubble size. Among the three ice layers, the increase rate of the surface layer was the highest, at approximately 0.017 mm per week ($r = 0.79$, $p < 0.05$). The corresponding values were 0.007 mm per week for the middle layer ($r = 0.67$, $p < 0.1$) and bottom layer ($r = 0.81$, $p < 0.05$). Notably, the increase rate of the surface layer was ~2.4 times that of the middle and bottom layers. Moreover, the mean size of the gas bubbles in the middle layer did not significantly change during the freezing phase, while the sizes of the gas bubbles in the surface and bottom layers notably increased.

The proportions of large bubbles in the three layers varied to different degrees (Figure 7b). The proportion in the surface layer generally increase during the observation period, at a rate of 9.1% per week ($r = 0.76$, $p < 0.05$). Similarly, the bottom layer exhibited an increasing trend, with a rate of 5.6% per week ($r = 0.66$, $p < 0.1$). In contrast, the trends observed for the middle layer differed. There was a consistent proportion of large gas bubbles, at 63.7±7.7%, with no significant trend. However, the mean size significantly increased. This may result from the merging of bubbles. This process exerted a greater impact on the mean bubble size than on the number of bubbles.

https://doi.org/10.5194/egusphere-2024-2155
Preprint. Discussion started: 19 August 2024

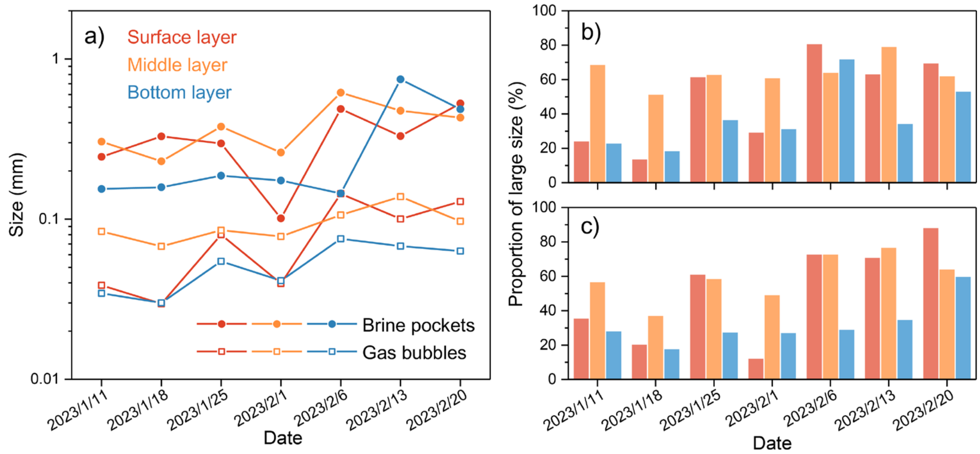

Figure 7: a) Temporal variations in the sizes of gas bubbles and brine pockets in the different ice layers. b) Variation in the proportion of large inclusions on each sampling date. A large inclusion was defined as an inclusion with a size larger than the median value.

Generally, there were increasing trends in the size of brine pockets in the three ice layers (Figure 7a). Furthermore, the increasing speeds were greater than those in the gas bubble size. From January 11 to February 20, the brine pocket size in the surface and middle layers increased nearly twofold, while that in the bottom layer increased nearly fourfold. Notably, this finding differed from the gas bubble observations. The differences in the brine pocket size between the surface and bottom layers were greater during the melting phase than during the freezing phase. In particular, the brine pocket size in the bottom layer remained almost constant during the freezing phase but rapidly increased during the melting phase.

The proportions of large brine pockets in the three layers typically increased during the observation period (Figure 6c). On January 11, the proportion of large brine pockets did not exceed 40%, and it increased to ~70% on February 20. Among the three layers, the increase rate of the surface layer was the greatest, at approximately 9.7% per week ($r = 0.72$, $p < 0.1$). The increase rates of the middle and bottom layers were 4.1% per week ($r = 0.66$, $p = 0.1$) and 4.7% per week ($r = 0.76$, $p < 0.05$), respectively. Although the proportions of large brine pockets in the bottom layer on February 13 and during the period from January 11 to February 6 were similar, the mean sizes differed. This was due to the maximum size of the brine pockets on February 13 greatly exceeding (~4 mm) that on the previous day (<1 mm) as a result of merging.

3.2.3 Merging of inclusions

Inclusions often merged with neighboring inclusions as they expanded, resulting in a decrease in the number density of inclusions of each size. Following Light et al. (2004), the merging factor (η = number density distribution after merging/original distribution) was used to quantify this process. Figure 8 shows the size distribution of gas bubbles and brine pockets on January 18 and February 13 as a function of the inclusion size and the corresponding η value. Note that the distributions were normalized according to their volume fraction. This indicates that the volume fractions of the inclusions

https://doi.org/10.5194/egusphere-2024-2155
Preprint. Discussion started: 19 August 2024

shown as solid lines in Figure 8 are identical, and the variation in η resulting from inclusion volume change was removed. These two dates were chosen because the difference in the proportion of large inclusions was significant (Figure 7b, c). The η values corresponding to other dates can be found in the following section.

Notably, the size distribution of gas bubbles on February 13 differed from that on January 18 (Figure 8a). On the one hand, the number of gas bubbles of each size decreased to different degrees. On the other hand, the maximum size of the gas bubbles clearly increased. There was also a common phenomenon between the bubble size distributions on the two dates. Although the number of gas bubbles of each size decreased, the size with the peak number density did not notably change. The corresponding size for the different ice layers was ~0.02 mm. The abovementioned differences and similarities reveal that the variations in the gas bubble size distribution from January 18 to February 13 did not result from the increase in bubbles of a single size class but rather from the merging of inclusions. Otherwise, the density number function would shift toward larger sizes and not notably decrease, as shown in Figure 8.

The η values of the gas bubbles in the three ice layers increased linearly (r > 0.9, $p < 0.001$) in the log(size)–log(number) space (Figure 8a). For gas bubbles with a size smaller than 0.01 mm, the number density decreased by more than 95% from January 18 to February 13. The decrease rate of gas bubbles larger than 0.2 mm reached ~40%. Notably, most merging occurred among the smaller bubbles. Among the three ice layers, the η value of the middle layer was the largest, while that of the surface layer was the smallest. This reveals that the merging rate of the gas bubbles in the middle layer was lower than that in the surface layer. This finding partially explains why the mean bubble size increased at a lower rate in the middle layer than in the surface layer (Figure 7a).

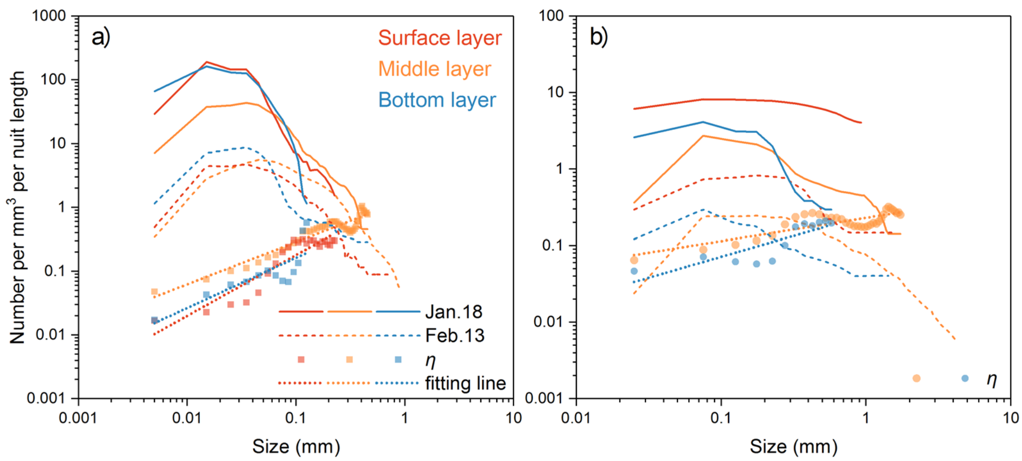

Figure 8: Size distribution of the a) gas bubbles and b) brine inclusions on January 18 and February 13 as a function of the inclusion size. The merging factors (η) of the gas bubbles and brine pockets between two dates are shown as squares and dots, respectively, and both are fitted by dotted lines.

Figure 8b shows the size distribution of brine pockets in the three ice layers on January 18 and February 13, along with the corresponding η value. Note that the η value of the surface layer is not shown here due to the insufficient number of brine

https://doi.org/10.5194/egusphere-2024-2155
Preprint. Discussion started: 19 August 2024

pockets observed in the ice surface layer, which resulted in a statistically nonsignificant fitting line of η. In general, the size distribution of the brine pockets varied similarly that of the gas bubbles, as did the η values of the brine pockets between the two dates. The η value for each brine pocket size was more similar than that for the gas bubbles. This suggests that brine pockets in ice are more diverse than gas bubbles, as the probability of merging brine pockets of the same size was greater than that of merging gas bubbles. This explains the greater increase in the brine pocket size than that in the gas bubble size (Figure 7a).

3.3 Drivers of the change in the microstructure of ice

The surface layer exhibited clearer variation in V_a than did the middle and bottom layers (Figure 5a). To analyze the mechanism underlying this variation, the potential influencing factors are shown in Figure 9a. The net shortwave radiation and surface ice temperature were observed (Sections 2.1 and 2.2), and the net longwave radiation was simulated (Section 2.2). The reason that the influencing factor of V_b was not analysed is that this parameter is directly controlled by the ice temperature and salinity. Therefore, V_b can be estimated using an ice thermodynamic model (Vancoppenolle et al., 2010). However, estimating the variation in V_a remains challenging due to a lack of information on its influencing factors.

There was no clear correlation between the net longwave radiation and V_a of the surface layer (Figure 9a), which was also observed for the surface temperature. However, a significant positive correlation was observed between the net shortwave radiation and V_a of the surface layer (r = 0.81, $p < 0.05$). With increasing net shortwave radiation, V_a of the surface layer gradually increased, with no clear surface temperature or surface elevation changes. This reveals that the increasing shortwave radiation absorbed by the ice surface was entirely used for phase changes. This process partially explains the formation of a porous sea ice surface layer (Macfarlane et al., 2023; Smith et al., 2022).

Figure 9b shows the variations in η of the gas bubbles in the middle layer with ice temperature change. Adopting an ice sample as the original condition, the ice temperature change between the other samples and the original sample could be obtained, as well as the corresponding η value. All the data were binned by ice temperature change. Significant relationships were found between the ice temperature changes and η of the middle layer for both small bubbles (r = -0.96, $p < 0.01$) and large bubbles (r = -0.79, $p < 0.05$). Notably, η decreased with increasing ice temperature. When the ice temperature was greater than 0°C, η was less than 1, indicating that the number density of gas bubbles decreased due to merging as the ice warmed. During the cooling phase, the number density of gas bubbles generally increased. This may have resulted from the newly formed bubbles separating from the solution.

Different phenomena were observed for the brine pockets (Figure 9c). The η values of the small and large brine pockets in the middle layer were significantly related to ice temperature changes (r = -0.97, $p < 0.01$ and r = -0.82, $p < 0.05$, respectively). Notably, η of the brine pockets was smaller than that of the gas bubbles for the same ice temperature changes. This reveals that the decreasing rate of the number density of brine pockets was greater than that of the gas bubbles during the warming phase. Moreover, the increasing rate of the number density during the cooling phase was lower. The former is

https://doi.org/10.5194/egusphere-2024-2155
Preprint. Discussion started: 19 August 2024

expected because brine pockets in ice are more varied than are gas bubbles (Figure 8). The latter may occur because the formation rate of new gas bubbles was greater than the dividing speed of brine pockets during the cooling phase.

No significant relationships were found between η of the inclusions in the surface or bottom layers and ice temperature changes (not shown here). The range of ice temperature changes in the bottom ice layer was smaller (-1 to 1°C) than that in the middle layer (-3 to 3°C), while the range in the surface layer was larger (-5 to 5°C). Therefore, the limitations of the observed temperature could be eliminated. This reveals that the changes or merging of inclusions in the surface and bottom layers mainly resulted from nonthermodynamic processes, such as those related to energy exchange with the atmosphere or ocean.

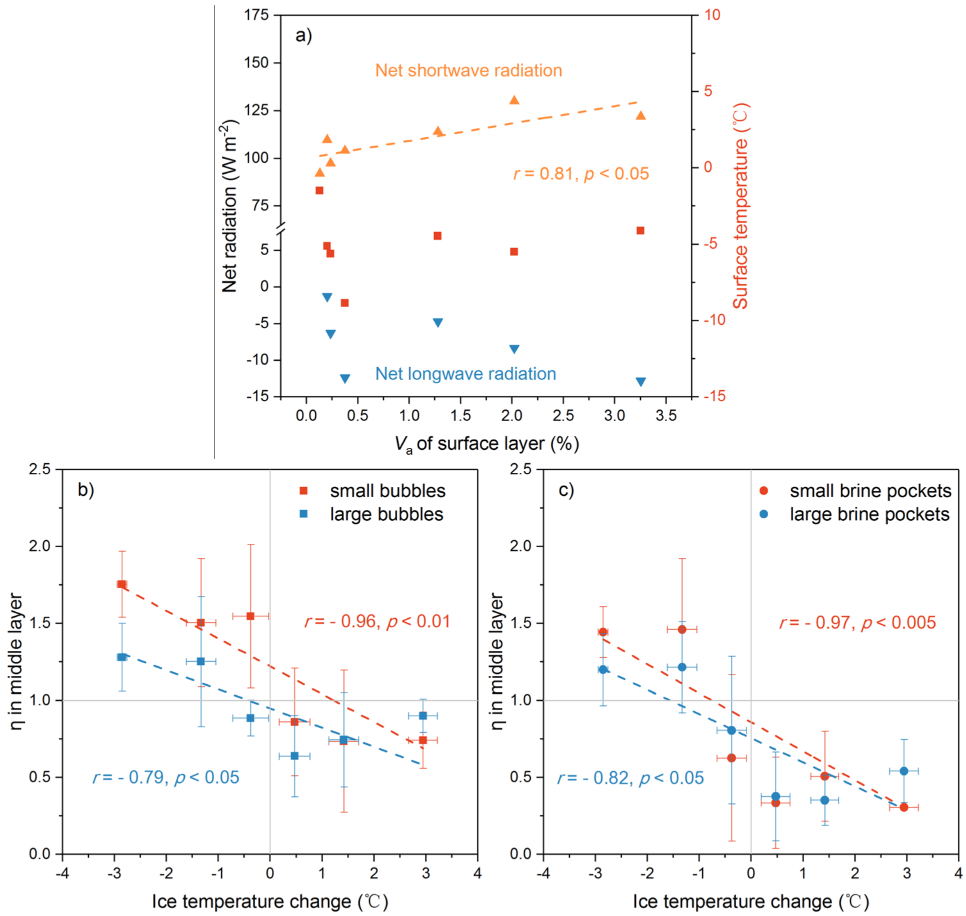

Figure 9: a) Relationships between V_a of the surface layer and the surface ice temperature, net longwave radiation, and net shortwave radiation. The variations in η of b) gas bubbles and c) brine pockets in the middle layer with ice temperature change.

https://doi.org/10.5194/egusphere-2024-2155
Preprint. Discussion started: 19 August 2024

4 Discussion

4.1 Uncertainties

4.1.1 Estimations of V_a and V_b

The uncertainties in V_a and V_b resulted from uncertainties in measuring T, S, and ρ_{ice} (Cox and Weeks, 1983; Leppäranta and Manninen, 1988). The uncertainties in T and S are known (Section 2.1). Therefore, to quantify the uncertainties in V_a and V_b, the uncertainty in ρ_{ice} was first evaluated. The focus here is on inherent uncertainties: the limiting measurement uncertainty and the errors related to brine loss.

The limiting measurement uncertainty in ρ_{ice} is defined as the sum of the maximum positive errors of all measurements. In this method (Equation 1), the limiting measurement uncertainty can be expressed as:

$$\Delta\rho_{ice} = \left|\frac{\partial\rho_{ice}}{\partial M_1}\right|\Delta M_1 + \left|\frac{\partial\rho_{ice}}{\partial M_2}\right|\Delta M_2 + \left|\frac{\partial\rho_{ice}}{\partial M_3}\right|\Delta M_3 \tag{7}$$

$$\frac{\Delta\rho_{ice}}{\rho_{ice}} = \left|\frac{(M_2-M_3)}{(M_2-M_1)(M_3-M_1)}\right|\Delta M_1 + \left|\frac{1}{M_2-M_1}\right|\Delta M_2 + \left|\frac{-1}{M_3-M_1}\right|\Delta M_3 \tag{8}$$

where ΔM_1, ΔM_2, and ΔM_3 of the present balance are 0.01 g. After inputting the means M_1, M_2, and M_3, the measurement uncertainty in the ice density can be obtained as 0.71%.

Brine loss during sampling is another significant factor contributing to uncertainty in ice density measurements. When an ice sample is removed from water, the brine in open channels is replaced by gas, which inevitably causes an increase in the gas content. This effect is particularly pronounced in the lower part of an ice core with high permeability. To accurately measure the ice density, it is important to account for brine channels that were drained during sampling. These channels are filled with liquid during submersion, and their volume should therefore be excluded from the measurements.

The mean V_b during the observation period was 3.8%. According to the relationship between the volume fraction of open brine and total brine from Maus et al. (2021), the open brine porosity of the present ice is 1.72%. Moreover, ρ_{ice} can be expressed as $(1 - V_a - V_b)\,\rho_i + V_b\,\rho_b$, where ρ_i is the density of pure ice (Cox and Weeks, 1983) and ρ_b is the density of brine (Equation 6). After inputting the mean V_a and ice temperature, ρ_{ice} without drainage was 0.917 g cm^{-3}. The ρ_{ice} value with drainage was 0.915 g cm^{-3}. Notably, the uncertainty due to drainage reached 0.203%. According to the propagation law of errors, the total uncertainty in ρ_{ice} was 0.74% (approximately 6.8×10^{-3} g cm^{-3}). This value agrees well with the reported uncertainty range for the hydrostatic weighing method (Pustogvar and Kulyakhtin, 2016).

As introduced in Section 2, the precision of the platinum resistance sensors employed in this observation study is 0.04°C. The uncertainty in the salinometer is 0.1‰. According to the phase diagrams (Cox and Weeks, 1983; Leppäranta and Manninen, 1988), the maximum absolute uncertainties in V_a and V_b reached 0.77% and 0.23%, respectively.

https://doi.org/10.5194/egusphere-2024-2155
Preprint. Discussion started: 19 August 2024

4.1.2 Effects of a changing temperature during imaging

The thin ice sections were imaged in a cold laboratory (-10°C) to observe their inclusions. This temperature is lower than the ice temperature (Figure 4). Experiments were designed by Light et al. (2003) to determine the thermal evolution of the ice microstructure over a wide range of temperatures. Their results showed that each inclusion decreased in size during the ice-cooling phase. In the experiment conducted by Light et al. (2003), the ice samples were maintained at each temperature for a minimum of 24 hours before photographs were obtained. In this study, ice sections were imaged after ice density measurement. The imaging time ranged from 15–25 min. Although the difference in time at low temperature is large, it is still necessary to analyze whether the low temperature during imaging affects the inclusion size.

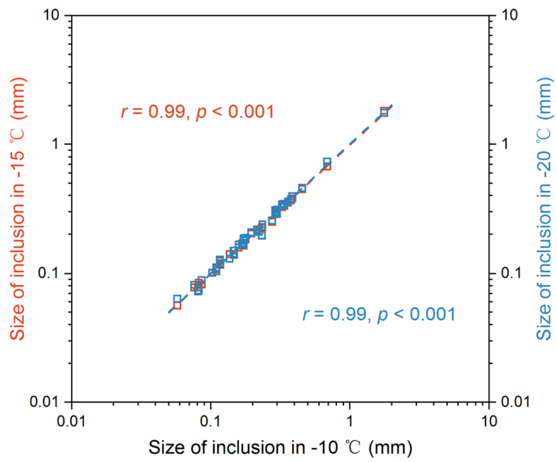

Figure 10: Comparison of inclusion sizes at different observed temperatures. The observed temperature was lowered by 5°C every half hour.

A sensitivity study was conducted to investigate whether inclusion size changes occur during short-term cooling. Thin ice sections were repeatedly imaged at -10°C, -15°C and -20°C. Each ice section was maintained at each temperature for 30 min before imaging. The measured inclusion sizes at each temperature are shown in Figure 10. There were significant linear relationships between the measured inclusion sizes (r = 0.99, p < 0.001), which revealed that short-term cooling did not clearly affect the inclusion size. The observed sizes at -10°C and -15°C differed by 2.5% ± 1.9%, while the difference reached 4.5% ± 3.4% between -10°C and -20°C. The corresponding lengths were 0.006 ± 0.008 mm and 0.009 ± 0.008 mm, respectively. These results indicated that short-term cooling does affect the inclusion size, with a greater effect observed under larger temperature differences. However, the effect is minimal and does not significantly impact the statistical results.

https://doi.org/10.5194/egusphere-2024-2155
Preprint. Discussion started: 19 August 2024

4.2 Comparison with other observations

This section provides a comparison of the inclusion sizes observed in this study with previous results. These earlier observations were conducted of Arctic sea ice and saline ice grown in artificial pools. It is challenging to consider all the potential influencing factors because the ice microstructure variations remain unclear. Figure 11a shows a comparison of the gas bubble size in this study with that in other studies as a function of the ice temperature. In comparison, the ice microstructure data of Light et al. (2003) and Perovich and Gow (2003) were obtained from first-year Arctic sea ice. Frantz et al. (2019) observed the microstructure of melting Arctic ice by computed tomography (CT). In Crabeck et al. (2016), ice was formed by freezing Arctic seawater in an in-ground concrete pool.

The bubble sizes in this study (0.003–3.2 mm) were consistent with previous results. The mean bubble sizes were close to those reported by Light et al. (2003), slightly smaller than those reported by Frantz et al. (2019), and smaller than those reported by Crabeck et al. (2016) and Perovich and Gow (1996). This study revealed more small bubbles than did previous studies, which could be attributed to differences in the observation resolution. Frantz et al. (2019) and Crabeck et al. (2016) obtained observations using CT. The resolution in the former study was 0.142 mm, while the resolution in the latter was 0.098 mm. Furthermore, the latter study observed a significant amount of snowice, which contained numerous large bubbles. The gas bubbles in Light et al. (2003) and Perovich and Gow (1996) were observed in images at resolutions of 0.002–0.003 and 0.03 mm, respectively. The resolution in this study ranged from 0.001–0.002 mm. At a low resolution, small bubbles may not be visible, yielding a larger mean size.

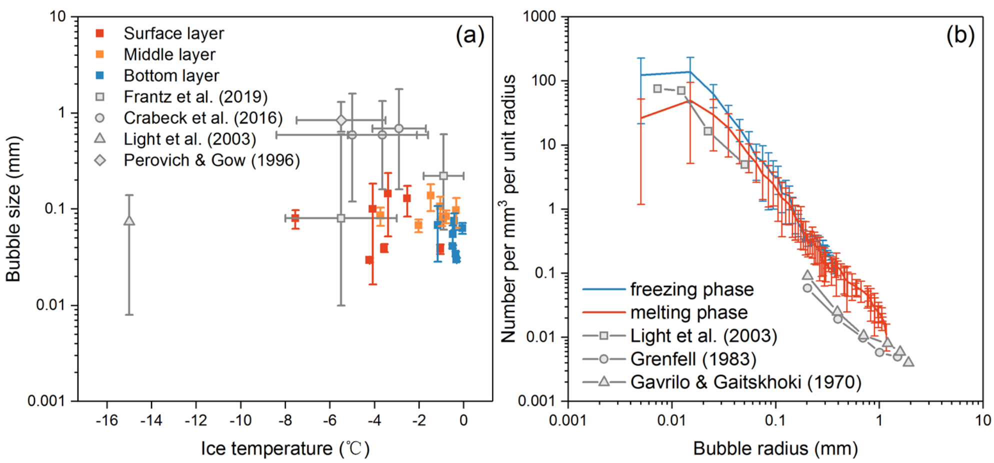

Figure 11: Comparison of the a) size and b) size distribution of gas bubbles between this study and related studies.

The bubble size distributions in this study suitably agreed with those in other studies (Figure 11b). The resolution of the gas bubble size distributions of freezing lead ice in Grenfell (1996) was 0.1 mm, while no small bubbles were detected. The mean V_a value in this ice (Section 3.2.1) is similar to the result (<1%) reported by Light et al. (2003). Therefore, the

https://doi.org/10.5194/egusphere-2024-2155
Preprint. Discussion started: 19 August 2024

comparison here is valid. Note that the horizontal axis in Figure 11 is the gas bubble radius and not the most commonly used diameter (e.g., Figure 8). In previous studies, the size distribution function of inclusions was consistently fitted by a power law, indicating that the number of inclusions increases with decreasing size. However, in this study, the minimum number of bubbles was small (Figure 8; Figure 11). This may be due to two reasons. First, small bubbles could not be fully observed, which causes a decrease in the number of minimum bubbles. The other reason is that the power law distribution is not appropriate. It is counterintuitive that the number of newly formed small bubbles is infinite. A Gaussian distribution may be more suitable for the size distribution, but this requires more accurate observations for confirmation.

The size of the brine pockets in this study ranged from 0.01–13 mm. Arcone et al. (1986) studied the microstructure of saline ice grown in an outdoor pool and obtained brine pocket sizes ranging from 0.04–1.68 mm (-30°C). Light et al. (2003) and Cole and Shapiro (1998) observed first-year Arctic ice, reporting brine pocket sizes of 0.01–8 mm at -15°C and 2.4 ± 2.5 mm at -14°C, respectively. Note that the smallest brine pocket measured by Cole and Shapiro (1998) was 0.1 mm. It is reasonable that the brine pocket size in this study is larger than that in other studies due to warmer ice (Section 3.1.3). In addition, the method in this study for identifying brine pockets (Section 2.3) may result in the classification of some small (< 0.02 mm) and round brine pockets as gas bubbles, resulting in underestimation of the number of small brine pockets. The bubble distribution in this study suitably agrees with that reported by Light et al. (2003) (Figure 11b). That's to say, the number of small gas bubbles was not notably overestimated. Therefore, it could be concluded that the methods used for classifying small inclusions in different works do not considerably affect the overall statistical results.

4.3 Mechanism of variations in ice inclusions

In this section, the mechanism of the variations in inclusions of different origins is examined according to the observations. The experiments were limited by the ice type. Although the salinity of saline ice in this study is less than that of typical sea ice, it is comparable to that of some estuaries along the coast and to that of sea ice in the Baltic Sea. Furthermore, the structural characteristics of ice closely resemble those of sea ice (Section 4.2). Therefore, the following discussion focuses not only on the present experimental results but also provides insights into the potential applications of sea ice.

4.3.1 Variations in the inclusion volume of the different layers

There was a significant increase in V_a of the surface layer during the melting phase (Figure 5a). Furthermore, this melting process occurred only on a microscopic scale and did not affect the ice surface elevation. As shown in Figure 5b, the equilibrium melting process could result in an increase in V_a smaller than 0.02%, which is considerably less than the actual increase in V_a (~3%). Although the observed ice surface temperature and porosity did not fully meet the commonly used empirical values (Eicken et al., 2004; Vancoppenolle et al., 2007), these newly formed bubbles likely resulted from flushing or similar processes. Figure 9a further shows the relationship between the net shortwave radiation and the flushing process. This figure partially justifies the assumption regarding the formation of a porous sea ice surface layer (Macfarlane et al., 2023; Smith et al., 2022).

https://doi.org/10.5194/egusphere-2024-2155
Preprint. Discussion started: 19 August 2024

The general trend in V_b/V_a of the middle layer closely approached the melting equilibrium trend (Figure 5b), indicating that the new bubbles in the middle layer were partially thermally driven. It is expected that other newly formed gas bubbles were driven by convection from the bottom layer given a sufficient ice porosity. During the melting phase, the increase in V_a of the bottom layer was only approximately 2% less than the thermally driven value. These bubbles partly accumulate in the middle layer as a result of their buoyancy, while others escape from the ice bottom. Moreover, it was found that for V_a <0.1%, V_b hardly affected V_a (refer to the enlarged part of Figure 5b). On the one hand, the ice temperature decreased from -0.8 to -4°C, and V_b decreased from 5.5 to 1.0% during this period. A decrease in the temperature could cause an increase in V_a by 0.5% due to gas release from cooled brine (Garcia and Gordon, 1992; Hamme and Emerson, 2004). Moreover, the latter could cause a decrease in V_a by 0.6% due to phase equilibrium. The two processes jointly result in a nearly constant bubble volume. On the other hand, it is also expected that some inactive gas bubbles occur in ice that are insensitive to V_b of ice.

4.3.2 Merging processes of inclusions

The variations in the inclusion volume in the middle layer are thermally driven, and the inclusion merging process is also thermally driven. Figure 9 shows significant relationships between the ice temperature difference and η of the middle layer. With ice warming, the number of inclusions decreases, and the size increases due to merging (Figure 7; Figure 8). However, there was no correlation between the ice surface temperature difference and the inclusion size distribution. Similarly, for the ice temperature and size distribution of bottom layer. These phenomena agree well with the results shown in Figure 5. The fitting relationship depicted in Figure 9 could be readily incorporated into the ice thermodynamic model. Other mechanisms remain needed to explain the merging of inclusions in the surface and bottom layers.

The merging equation obtained in this study differed from that used by Light et al. (2004). In their study, η was assumed to vary linearly in the log(volume) and log(number) spaces, which is supported by our observations (Figure 8). Furthermore, in their parameterization, η was set to 1 for the smallest inclusions, and the most merging was predicted to occur among larger inclusions. However, in this study, the merging of small inclusions was more notable than that of large inclusions (Figure 8). Currently, it is unclear whether this difference is the result of differences in ice types. Our findings conform with intuition, as the number of small inclusions exceeded that of larger inclusions, and the likelihood of additional nearby inclusions was greater.

The sensitivity of η to the ice temperature also differed between this study and that of Light et al. (2004). In their study, η was 1 at -14°C and 0.1 at -1°C, with a decrease of 0.07 per °C. The minimum observed ice temperature in this study was -7.5°C. Therefore, it is unclear whether merging will stop at lower ice temperatures. The observed decreasing rates of η for small and large gas bubbles were 0.18 and 0.12 per °C, respectively. The corresponding values for small and large brine pockets were 0.19 and 0.16 per °C, respectively. Notably, the merging rate in this study was much greater than that reported by Light et al. (2004), although the salinity was much lower. Furthermore, the variations in the inclusion volume were eliminated herein. If the increase in the inclusion volume were considered, the merging rate would be even greater.

https://doi.org/10.5194/egusphere-2024-2155
Preprint. Discussion started: 19 August 2024

4.3.3 Variations in inclusions of different sizes

Although small inclusions exhibit a greater probability of merging than do large inclusions (Figure 8), the merging of large inclusions more notably impacts the mean inclusion size. For example, the merging of two 0.01-mm inclusions into one 0.02-mm inclusion imposes a negligible effect on the mean size compared to the merging of two 1-mm inclusions into one 2-mm inclusion. This occurs because the effects on the number of inclusions are identical. The number of large gas bubbles in the middle layer is greater than that in the surface and bottom layers (Figure 6b). That is, the probability of gas bubbles merging in the middle layer is lower than that in the other layers. Consequently, the change in the size distribution in the middle layer is smaller than that in the other layers (Figure 8a), but the change in the mean size remains notable (Figure 7a). This explains why the proportion of large bubbles in the middle layer remains relatively constant, while the mean size continues to increase (Figure 7a, b).

In summary, the merging of large inclusions imposes a smaller influence on the size distribution but more notably influences the mean size than small inclusions. This partly explains why Light et al. (2004) only considered the merging of large inclusions but were still able to accurately estimate the reduced ice scattering coefficient due to merging. In addition, it is expected that large inclusions formed during freezing will maintain their relatively large sizes in the subsequent melting process. In other words, the banding features associated with microstructural gas and brine porosity variations (Cole et al., 2004) can hardly be easily altered during ice melting.

5 Summary and conclusions

The field work was designed to obtain information for providing a fundamental understanding of the variations in the size distribution of ice inclusions during the ice freezing or melting phase. Ice cores sampled from a saline lake adjacent to the Bohai Sea were analyzed weekly to study the ice microstructure and physical properties. High-resolution imagery was used to quantify the size and distribution of inclusions within ice.

The microstructure of ice continuously changes during both the growth and melting phases. Notably, V_a of ice remained relatively constant during the freezing phase but significantly increased during the melting phase. Similarly, V_b of ice significantly increased during the melting phase but decreased during the freezing phase. The general trend in V_b/V_a of the middle layer was much closer to melting equilibrium trend, which revealed that the newly formed bubbles in the middle layer were partly thermally driven. For the ice surface layer, V_a notably increased, with only a slight variation in V_b. A significant relationship between the net shortwave radiation and V_a of the surface layer was observed. It is suggested that the newly formed bubbles were a result of flushing or a similar process.

There was a general increasing trend in the inclusion size during the ice melting phase because of the increased proportion of large inclusions. The changes in the brine pocket size during the freezing phase were not as notable as those during the melting phase. Therefore, the gas bubble size in the middle layer decreased. Moreover, the gas bubble size in the surface and bottom layers clearly increased during the freezing phase. These changes were the result of merging. The merging factor η of the inclusions linearly increased in the log(size)–log(number) space. Notably, most merging occurred among smaller inclusions. Furthermore, η of the middle layer was significantly affected by the ice temperature difference. With the warming of ice, the number density of inclusions generally decreased due to merging. The η value of inclusions in the surface or bottom layers are insensitive to ice temperature differences, which reveals that other mechanisms control their merging processes.

This study provided new insights into microstructural changes during ice growth and decay, which represent the microscale effects of varying circumstances on ice. However, additional processes that require further investigation, such as the relationship between newly formed inclusions and the gas saturation level or growth velocity. They are needed to better understand ice microstructural changes and their subsequent effects on other optical and thermodynamic properties of ice.

Acknowledgements. This study was supported by the National Key R&D Program of China (2023YFC2809102), the National Natural Science Foundation of China (42320104004, 42276242), the Postdoctoral Fellowship Program of CPSF (GZB20230102), the Joint Funds of the National Natural Science Foundation of Liaoning Province (2023-BSBA-021).

Author contributions. Miao Yu: Investigation, Methodology, Formal analysis, Writing – original draft. Peng Lu: Supervision, Conceptualization. Hang Zhang, Fei Xie: Investigation. Lei Wang, Qingkai Wang, Zhijun Li: review & editing.

Data Availability Statement. The data applied in this work can be accessed by the link: https://doi.org/10.5281/zenodo.12540064

Competing interests. The authors declare that they have no known competing financial interests or personal relationships that could have appeared to influence the work reported in this paper.

https://doi.org/10.5194/egusphere-2024-2155
Preprint. Discussion started: 19 August 2024

References

Arcone, S., Gow, A. and McGrew, S.: Structure and dielectric properties at 4.8 and 9.5 GHz of saline ice. Journal of Geophysical Research: Oceans, 91(C12): 14281-14303, http://doi.org/10.1029/JC091iC12p14281, 1986.

Bailey, D., Holland, M., DuVivier, A., Hunke, E. and Turner, A.: Impact of a new sea ice thermodynamic formulation in the CESM2 sea ice component. Journal of Advances in Modeling Earth Systems, 12(11), http://doi.org/10.1029/2020MS002154, 2020.

Cole, D. and Shapiro, L.: Observations of brine drainage networks and microstructure of first-year sea ice. Journal of Geophysical Research: Oceans, 103(C10): 21739-21750, http://doi.org/10.1029/98JC01264, 1998.

Cole, D., Eicken, H., Frey, K. and Shapiro, L.: Observations of banding in first-year Arctic sea ice. Journal of Geophysical Research: Oceans, 109(C8), http://doi.org/10.1029/2003JC001993, 2004.

Corkill, M., Moreau, S., Janssens, J., Fraser, A. D., Heil, P., Tison, J., et al.: Physical and Biogeochemical Properties of Rotten East Antarctic Summer Sea Ice. Journal of Geophysical Research: Oceans, 128(2), http://doi.org/10.1029/2022JC018875, 2023.

Cox, G. and Weeks, W.: Equations for determining the gas and brine volumes in sea-ice samples. Journal of Glaciology, 29(102): 306-316, http://doi.org/10.3189/S0022143000008364, 1983.

Cox, G. and Weeks, W.: Numerical simulations of the profile properties of undeformed first-year sea ice during the growth season. Journal of Geophysical Research: Oceans, 93(C10): 12449-12460, http://doi.org/10.1029/JC093iC10p12449, 1988.

Crabeck, O., Delille, B., Rysgaard, S., Thomas, D. N., Geilfus, N., Else, B., et al.: First "in situ" determination of gas transport coefficients (DO2, DAr, and DN2) from bulk gas concentration measurements (O2, N2, Ar) in natural sea ice. Journal of Geophysical Research: Oceans, 119(10): 6655-6668, http://doi.org/10.1002/2014JC009849, 2014.

Crabeck, O., Galley, R., Delille, B., Else, B., Geilfus, N., Lemes, M., et al.: Imaging air volume fraction in sea ice using non-destructive X-ray tomography. The Cryosphere, 10(3): 1125-1145, http://doi.org/10.5194/tc-10-1125-2016, 2016

Crabeck, O., Galley, R. J., Mercury, L., Delille, B., Tison, J., Rysgaard, S.: Evidence of freezing pressure in sea ice discrete brine inclusions and its impact on aqueous-gaseous equilibrium. Journal of Geophysical Research: Oceans, 124(3): 1660-1678, http://doi.org/10.1029/2018JC014597, 2019.

Crawford, T. and Duchon, C.: An Improved Parameterization for Estimating Effective Atmospheric Emissivity for Use in Calculating Daytime Downwelling Longwave Radiation. Journal of applied meteorology (1988), 38(4): 474-480, http://doi.org/10.1175/1520-0450(1999)038<0474:AIPFEE>2.0.CO;2, 1999.

Duarte, H., Dias, N. and Maggiotto, S.: Assessing daytime downward longwave radiation estimates for clear and cloudy skies in Southern Brazil. Agricultural and Forest Meteorology, 139(3-4): 171-181, http://doi.org/10.1016/j.agrformet.2006.06.008, 2006.

Efimova, N.: On methods of calculating monthly values of net longwave radiation. Meterol Gidrol, 10: 28-33, 1961.

https://doi.org/10.5194/egusphere-2024-2155
Preprint. Discussion started: 19 August 2024

Eicken, H.: Chapter 2: From the microscopic to the macroscopic to the regional scale: Growth, microstructure and properties of sea ice. In D. N. Thomas, & G. S. Dieckmann (Eds.), Sea ice: An introduction to its physics, chemistry, biology and geology. Blackwell Science, London, pp. 22-81, 2003.

Eicken, H., Grenfell, T., Perovich, D., Richter Menge, J., Frey, K.: Hydraulic controls of summer Arctic pack ice albedo. Journal of Geophysical Research: Oceans, 109(C8), http://doi.org/10.1029/2003JC001989, 2004.

Frantz, C., Light, B., Farley, S., Carpenter, S., Lieblappen, R., Courville, Z., et al.: Physical and optical characteristics of heavily melted "rotten" Arctic sea ice. The Cryosphere, 13(3): 775-793, http://doi.org/10.5194/tc-13-775-2019, 2019.

Garcia, H., Gordon, L.: Oxygen solubility in seawater: Better fitting equations. Limnology and Oceanography, 37(6): 1307-1312, http://doi.org/10.4319/lo.1992.37.6.1307, 1992.

Grenfell, T.: A theoretical model of the optical properties of sea ice in the visible and near infrared. Journal of Geophysical Research: Oceans, 88(C14): 9723-9735, http://doi.org/10.1029/JC088iC14p09723, 1983.

Hamme, R., Emerson, S.: The solubility of neon, nitrogen and argon in distilled water and seawater. Deep Sea Research Part I: Oceanographic Research Papers, 51(11): 1517-1528, http://doi.org/10.1016/j.dsr.2004.06.009, 2004.

Hruba, J., and Kletetschka, G.: Environmental record of layers of bubbles in natural pond ice. Journal of Glaciology, 64(248): 866-876, http://doi.org/10.1017/jog.2018.73, 2018.

Hunke, E., Notz, D., Turner, A., Vancoppenolle, M.: The multiphase physics of sea ice: a review for model developers. The Cryosphere, 5(4): 989-1009, http://doi.org/10.5194/tc-5-989-2011, 2011.

Leppäranta, M., and Manninen, T.: The brine and gas content of sea ice with attention to low salinities and high temperature, Finnish Institute for Marine Research Internal Report, Helsinki, Finnish, 1988, 15 pp., 1988.

Light, B., Grenfell, T., and Perovich, D.: Transmission and absorption of solar radiation by Arctic sea ice during the melt season. Journal of Geophysical Research, 113: C03023: http://doi.org/10.1029/2006JC003977, 2008.

Light, B., Maykut, G. and Grenfell, T.: Effects of temperature on the microstructure of first-year Arctic sea ice. Journal of Geophysical Research: Oceans, 108(C2): 3051, http://doi.org/10.1029/2001JC000887, 2003.

Light, B., Maykut, G. and Grenfell, T.: A temperature-dependent, structural-optical model of first-year sea ice. Journal of Geophysical Research, 109: C06013, http://doi.org/10.1029/2003JC002164, 2004.

Macfarlane, A., Dadic, R., Smith, M., Light, B., Nicolaus, M., Henna-Reetta, H., et al.: Evolution of the microstructure and reflectance of the surface scattering layer on melting, level Arctic sea ice. Elementa: Science of the Anthropocene, 11(1), http://doi.org/10.1525/elementa.2022.00103, 2023.

Maus, S., Schneebeli, M. and Wiegmann, A.: An X-ray micro-tomographic study of the pore space, permeability and percolation threshold of young sea ice. The Cryosphere, 15(8): 4047-4072, http://doi.org/10.5194/tc-15-4047-2021, 2021.

Maykut, G. and Light, B.: Refractive-index measurements in freezing sea-ice and sodium chloride brines. Applied Optics, 34(6): 950, http://doi.org/10.1364/AO.34.000950, 1995.

https://doi.org/10.5194/egusphere-2024-2155
Preprint. Discussion started: 19 August 2024

Meyers, T. and Dale, R.: Predicting Daily Insolation with Hourly Cloud Height and Coverage. Journal of Applied Meteorology and Climatology, 22(4): 537-545, http://doi.org/10.1175/1520-0450(1983)022<0537:PDIWHC>2.0.CO;2, 1983.

Notz, D. and Worster, M. In situ measurements of the evolution of young sea ice. Journal of Geophysical Research, 113: C03001, http://doi.org/10.1029/2007JC004333, 2008.

Oggier, M. and Eicken, H. Seasonal evolution of granular and columnar sea ice pore microstructure and pore network connectivity. Journal of Glaciology: 1-16, http://doi.org/10.1017/jog.2022.1, 2022.

Otsu, N.: A Tlreshold Selection Method from Gray-Level Histograms. IEEE Transactions on Systems, Man, and Cybernetics, 9(1): 62-66, http://doi.org/10.1109/TSMC.1979.4310076, 1979.

Perovich, D. and Gow, A.: A quantitative description of sea ice inclusions. Journal of Geophysical Research, 101(C8): 18327-18343, http://doi.org/10.1029/96JC01688, 1996.

Petrich, C. and Eicken, H.: Chapter 1: Overview of sea ice growth and properties. In David N Thomas (Ed.), Sea ice. 3rd ed. John Wiley & Sons, Chichester, UK; Hoboken, NJ, pp. 1-41, 2017.

Pringle, D., Miner, J., Eicken, H. and Golden, K.: Pore space percolation in sea ice single crystals. Journal of Geophysical Research: Oceans, 114(C12), http://doi.org/10.1029/2008JC005145, 2009.

Pustogvar, A. and Kulyakhtin, A.: Sea ice density measurements. Methods and uncertainties. Cold Regions Science and Technology, 131: 46-52, http://doi.org/10.1016/j.coldregions.2016.09.001, 2016.

Ridler, T. and Calvard, S.: Picture Thresholding Using an Iterative Selection Method. IEEE Transactions on Systems, Man, and Cybernetics, 8(8): 630-632, http://doi.org/10.1109/tsmc.1978.4310039, 1978.

Salganik, E., Lange, B., Katlein, C., Matero, I., Anhaus, P., Muilwijk, M., et al.: Observations of preferential summer melt of Arctic sea-ice ridge keels from repeated multibeam sonar surveys. The Cryosphere, 17(11): 4873-4887, http://doi.org/10.5194/tc-17-4873-2023, 2023.

Salomon, M., Maus, S. and Petrich, C.: Microstructure evolution of young sea ice from a Svalbard fjord using micro-CT analysis. Journal of Glaciology, 68(269): 571-590, http://doi.org/10.1017/jog.2021.119, 2022.

Smith, M., Light, B., Macfarlane, A., Perovich, D., Holland, M., Shupe, M.: Sensitivity of the Arctic sea ice cover to the summer surface scattering layer. Geophysical Research Letters, 49(9), http://doi.org/10.1029/2022GL098349, 2022.

Trodahl, H., Wilkinson, S., McGuinness, M. and Haskell, T.: Thermal conductivity of sea ice; dependence on temperature and depth. Geophysical Research Letters(7): 1279-1282, http://doi.org/10.1029/2000GL012088, 2001.

Tsurikov, V.: The formation and composition of the gas content of sea ice. Journals of glaciology, 22(86): 67-81, http://doi.org/10.1017/S0022143000014064, 1979.

Turner, A. and Hunke, E.: Impacts of a mushy-layer thermodynamic approach in global sea-ice simulations using the CICE sea-ice model. Journal of Geophysical Research: Oceans, 120(2): 1253-1275, http://doi.org/10.1002/2014JC010358, 2015.

Vancoppenolle, M., Goosse, H., de Montety, A., Fichefet, T., Tremblay, B., Tison, J.: Modeling brine and nutrient dynamics in Antarctic sea ice: The case of dissolved silica. Journal of Geophysical Research, 115: C02005, http://doi.org/10.1029/2009JC005369, 2010.

Vancoppenolle, M., Bitz, C. and Fichefet, T.: Summer landfast sea ice desalination at Point Barrow, Alaska: Modeling and observations. Journal of Geophysical Research: Oceans, 112(C4), http://doi.org/10.1029/2006JC003493, 2007.

Wang, Q., Lu, P., Leppäranta, M., Cheng, B., Zhang, G., Li, Z., Physical properties of summer sea ice in the pacific sector of the Arctic during 2008–2018. Journal of Geophysical Research: Oceans, 125(9), http://doi.org/10.1029/2020JC016371, 2020.

Xie, F., Lu, P., Li, Z., Wang, Q., Zhang, H., Zhang, Y.: A floating remote observation system (FROS) for full seasonal lake ice evolution studies. Cold Regions Science and Technology, 199, http://doi.org/10.1016/j.coldregions.2022.103557, 2022.